manchester
particle physics

MAN/HEP/94/01
30 Nov 1994

The OPAL Muon Barrel Detector

R.J.Akers, J.Allison, P.Ashton, G.A.Bahan, J.T.M.Baines, J.N.Banks, R.J.Barlow, S.Barnett, C.Beeston, J.T.M.Chrin, S.G.Clowes, O.W.Davies, I.P.Duerdoth, P.S.Hinde, R.E.Hughes-Jones, G.D.Lafferty, F.K.Loebinger, A.A.Macbeth, R.F.McGowan, M.W.Moss, P.G.Murphy, B.Nijjhar, A.J.P.O'Dowd, S.J.Pawley, P.D.Phillips, G.E.Richards, A.Skillman, K.Stephens, N.J.Tresillian, N.C.Wood, T.R.Wyatt.

Department of Physics and Astronomy,

The University of Manchester, Manchester, M13 9PL

Abstract

The barrel part of the OPAL muon detector consists of 110 drift chambers forming four layers outside the hadron absorber. Each chamber covers an area of 1.2 m by up to 10.4 m and has two cells with wires parallel to the beam and a drift distance of 297 mm. A detailed description of the design, construction, operation and performance of the sub-detector is given. The system has been operating successfully since the start of LEP in 1989.

(Submitted to Nucl. Instr. and Meth.)

1 Introduction

OPAL [1, 2] is one of the four detectors built for the e^+e^- storage ring LEP at CERN. It is a multipurpose apparatus with an excellent acceptance for Z^0 decays over a solid angle of nearly 4π and consists of several sub-detectors which attempt to measure and identify all the emerging particles from the collisions. As muons interact only weakly and electromagnetically and are more massive than electrons they have a larger range than other charged particles and are identified as tracks outside an absorber. The OPAL muon detector has almost 4π coverage and this is divided into a barrel region (described in this paper) and an endcap region [3]. Identification of muons in events of the type $e^+e^- \to \mu^+\mu^-$ is not problematical because there is a single track in each of several sub-detectors and indeed these events are useful for understanding the muon detector. The challenge comes in identifying the muons in events in which the Z^0 decays hadronically and the muon has to be separated from a background of hadrons. Such events are of particular physics interest because, while decays via light quarks do not give prompt muons, decays via heavy quarks, in particular b quarks, do. An important route to b physics is by identifying the muons. Relevant features of a muon detector are solid angle coverage, efficiency of finding muons, purity of the muon sample and rejection of hadronic background.

This paper describes in detail the muon barrel sub-detector of OPAL; it consists of several large area drift chambers. These are the product of a number of years of research and development at the University of Manchester, which has had a long-standing involvement in muon detection in particle physics experiments at PETRA, LEP and HERA. The chamber design is a development of the JADE muon chambers [4, 5], but is characterised by larger area, greater drift distance, improved position resolution in the drift direction, and most significantly by the incorporation of diamond shaped cathode pads which give the longitudinal coordinate, z [6]. Thus the chambers measure space points.

The OPAL muon barrel chambers have been in operation at LEP since August 1989 and over 4×10^6 Z^0 decays have been recorded and analysed, resulting in good understanding of their reliability and performance.

The relevant parts of the OPAL detector are briefly described in section 2 and more details of the principles and problems of muon identification are given in section 3. The bulk of the paper. section 4 describes the design of the chambers. their detailed construction including support. survey. gas system, high voltage system. electronics, 'z algorithm', data acquisition. trigger. and monitoring. The software, in particular the pulse finding and the analysis for the coarse. medium and fine z. is described in section 5. Section 6 deals with the important topic of calibration and finally section 7 outlines the performance in OPAL itself. To recap, the task of the sub-detector is to identify muons by measuring their position and direction behind the hadron absorber.

2 OPAL

The essential parts of the OPAL [1, 2] detector (see fig 1) are the central tracking chambers operating in a solenoidal magnetic field of 0.435 T. a lead glass electromagnetic calorimeter, a hadron calorimeter and the muon detector. The central tracking includes a large pictorial drift chamber. some 4 m long and almost 2 m in radius, as well as a vertex drift chamber. a microvertex silicon detector (installed in 1991) and a Z-chamber. Also there is a time-of-flight scintillation hodoscope, presamplers for the barrel and endcap electromagnetic calorimeters and forward detectors which measure the luminosity.

The hadron calorimeter includes the iron of the return yoke and is segmented with layers of limited streamer tubes which give a measurement of the energy of a hadronic shower. It also assists in the identification of muons. The thickness of iron is determined by the calorimeter requirements, and the iron is not magnetically saturated. For $|\cos\theta|<0.35$ there is an additional collar of iron. 0.2 m thick needed to improve the absorption of hadrons.

The entire iron structure is surrounded by the muon detector. The bend in the central solenoidal magnetic field combined with that in the return yoke means that tracks of all momenta emerge approximately radially [7]. Where physically possible there are four layers of chambers both in the barrel and the endcap. Of the full solid angle, 93% is covered by at least one layer of detector – there are gaps, inevitably, due to the beam pipe (2×0.8%). the support legs (2×2.2%). and cables (2×0.6%). The barrel part of the detector covers $|\cos\theta|<0.69$ for four layers and $|\cos\theta|<0.72$ for one or more layers. The acceptance of the endcap part of the detector overlaps with that of the barrel and starts at about $|\cos\theta|=0.65$ (see fig 2).

The iron of the return yoke provides 4 or more interaction lengths of absorber over a solid angle of 97% of 4π, and the other sub-detectors. especially the lead glass of the electromagnetic calorimeter. also contribute to the amount of absorber. Over nearly all of this solid angle the amount of material that a particle has to traverse exceeds 1.3 m of iron equivalent (over 7 interaction lengths for pions) (see fig 3). This is required to reduce the probability of a pion not interacting to less than 0.001.

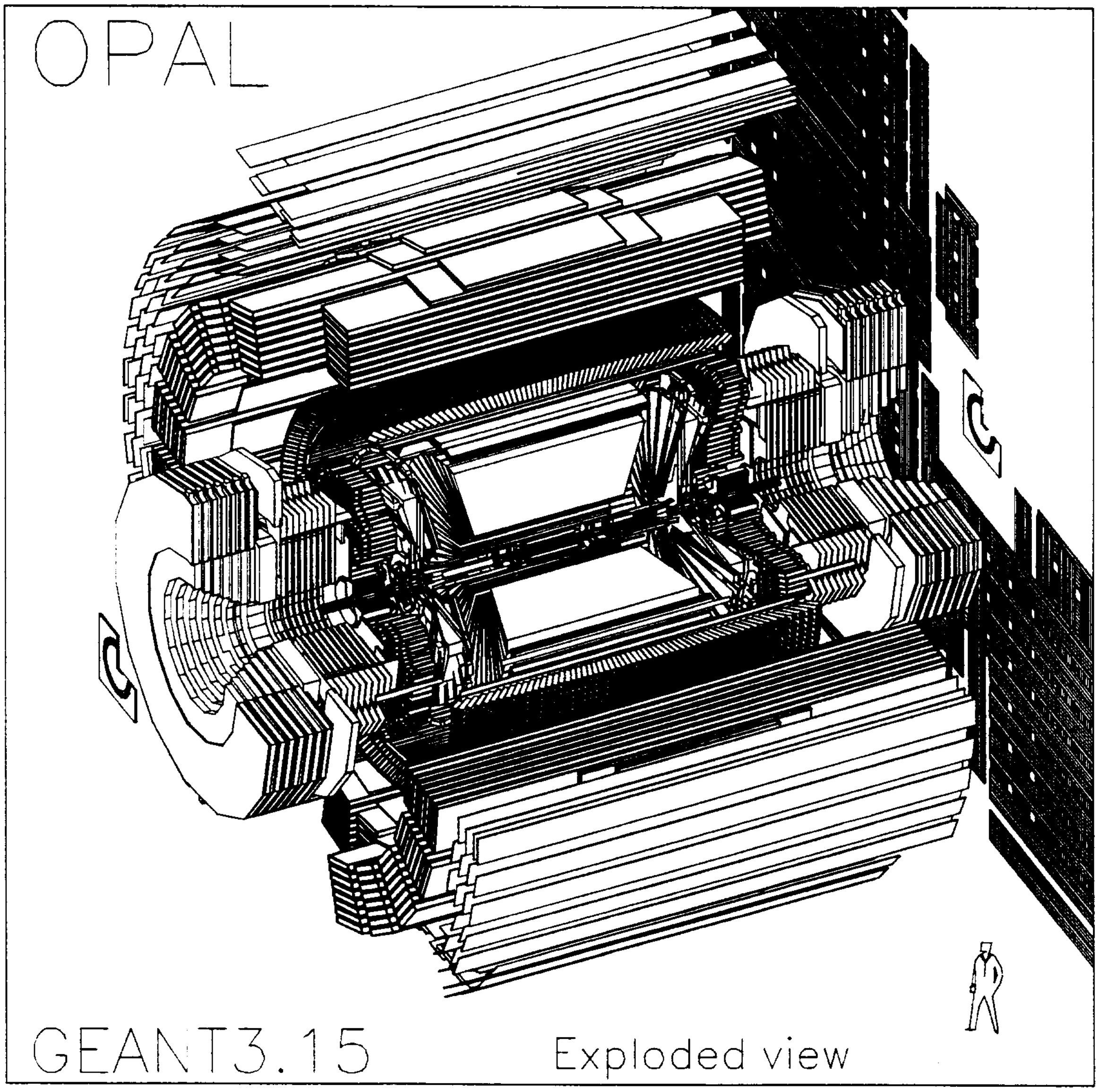

Figure 1: Overview of the OPAL detector.

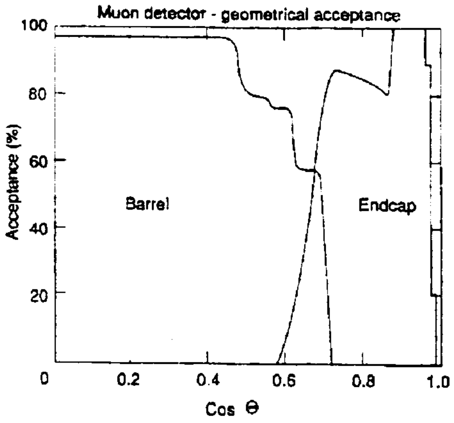

Figure 2: Geometrical acceptance of the muon detectors (requiring 3 layers) as a function of cosθ, averaging over ϕ.

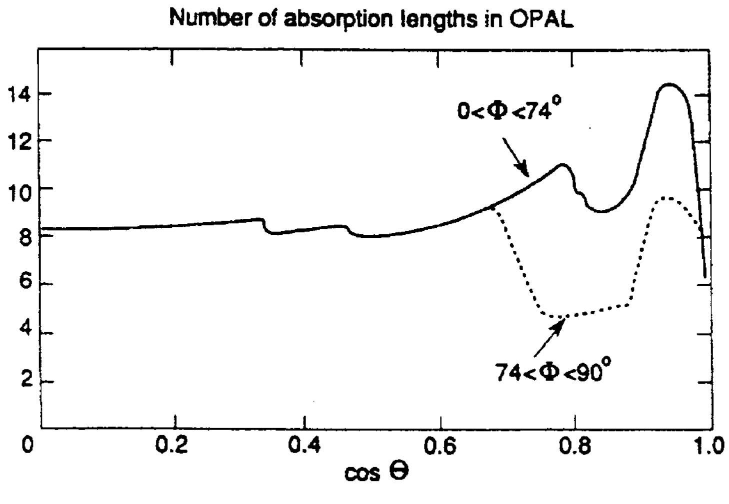

Figure 3: Total amount of material (in absorption lengths) that a particle has to penetrate in order to reach the muon chambers, as a function of cosθ, and averaged over the indicated ϕ ranges, as determined from Monte Carlo simulation.

3 Muon identification

At LEP I, the maximum momentum of the muons is 46 GeV, and at LEP II it will be even higher. However, most of the muons of interest, those coming from hadron decay, have much lower momentum, typically about 5 GeV. Ideally, all muons emerge from the absorber and all other particles are stopped so that every track is clean and is a muon. In practice, muons below some cutoff momentum range out and hadrons produce a background. Three processes can be identified by which a hadron can fake a muon: sneakthrough, which is a failure to interact strongly and depends exponentially on the absorber thickness: punchthrough, in which the hadron interacts but secondary particles emerge and fake a muon, and decay in flight of pions and kaons to muons. Decay is important at low momenta and punchthrough at high momenta. Some of the kaon and pion decays may be identified as kinks or mismatches in the central jet chamber. Also there may be cracks in the absorber where the amount of material is low.

The muon detector does not make a measurement of the momentum of the tracks and there is no absorber between its planes. However the hadron calorimeter is segmented and this aids in the identification of muons.

Muon identification relies on extrapolating the track seen in the central detector through the absorber, allowing for energy loss and multiple coulomb scattering, and looking for a track in the muon detector which matches in position and angle in two views. The positional and angular accuracies required for the track measurement are determined by the multiple coulomb scattering of the highest energy muons of interest and are about 2 mm and 3 mrad respectively. Monte Carlo simulations [8] suggested that background rejection is improved by measuring both coordinates; it continues to improve as the spatial and angular resolutions improve to about 2 mm and 3 mrad respectively, but thereafter any further improvement in resolution produces negligible improvement in the background rejection. In order to provide sufficient redundancy the design calls for emerging tracks, where possible, to pass through a minimum of four layers of detector. The amount of absorbing material is a compromise between cost, background reduction and the cut-off at low momentum due to range-out.

4 Drift Chambers

4.1 Basic design

The design requirements of the detector are to cover a cylinder of length 10 m and radius 5 m, i.e. an area of about 300 m^2, and to measure space points with an accuracy of better than 2 mm and directions with an accuracy of better than 3 mrads in both the r-z and the x-y views. To achieve the required angular resolution (without a further improvement in spatial resolution) a total spacing of about 600 mm is needed. The obvious technology is drift chambers but limited streamer tubes were also considered. The signal rate per unit area is modest; of the order of 0.01 $m^{-2}s^{-1}$ and allowing for a background of about 100 $m^{-2}s^{-1}$ (consisting mainly of chamber noise with small contributions from cosmics and hadronic leakage) it is possible to drift a large distance (297 mm was chosen) even with wires which are 10 m long. Moreover the maximum drift time, about 8 μs, is well within the bunch-bunch time of LEP, i.e. 11 μs when operating with eight bunches on eight bunches.

All the drift chambers are orientated with their wires nominally parallel to z and with the drift direction approximately perpendicular to the emerging tracks. Thus in the x-y view the tracks are approximately perpendicular to the chamber planes and there are no angle effects contributing to the drift time. In the r-z view the tracks pass through the chambers either normally (in the middle) or at angles up to 45° (at the ends) and this spreads the avalanches out along the wire. In order to resolve left-right ambiguities, to fit tracks with a constraint and to provide some redundancy in the case of failure it was decided that four layers were necessary. There is no particular requirement to minimise the thickness of the chambers.

The chambers are read out by two VME based computer systems which process the data and pass them on to the OPAL data acquisition network. These VME computers also control and monitor the high voltage. A dedicated VAXstation samples events from the VME system, monitors the detector and determines calibration constants which are stored in the OPAL calibration data base, OPCAL. An independent network of VME computer systems, the OPAL Slow Controls [9], monitors the gas system as well as general safety in OPAL and gives warning of anomalies.

4.2 Drift chambers

There are 110 large area drift chambers in the barrel part of the OPAL muon detector. Each chamber is 1.2 m wide and 90 mm deep; (this includes the integral support frame). 44 chambers are mounted on each side of the barrel, 10 in the top module and 12 in the bottom module (see fig 4). 70 of the chambers are the maximum length that OPAL allows, 10.4 m, but shorter chambers are required to fit between the legs and cable runs, so 20 are only 8.4 m and another 20 are 6.0 m. Except for their different lengths the construction and cross section (see fig 5) of the chambers are identical.

The chambers in the four layers are staggered by typically 50 mm in the φ direction with respect to each other – firstly to resolve the left-right ambiguities when tracks are fitted, and secondly to provide drift time checksums which are sensitive to the drift velocity and relative positions. Thus the chambers are to some extent self calibrating. The chambers have very little dead area; the sensitive area extends to 20 mm of the edge. In the outer layer the chambers simply butt against their neighbours and in the other layers there is an overlap of typically 50 mm.

Each chamber consists of two cells, side by side, each containing an anode wire (50 μm in diameter) running the whole length of the chamber and supported every 1.4 m. Electrons drift a maximum distance of 297 mm from either side. The sensitive volume is defined by two printed circuit boards with a nominal gas gap of 15 mm. The largest PC boards commercially available [10] were 4 feet by 12 feet and this constraint determined the actual width of the chambers. The outside of the PC boards is copper clad and is at ground potential, as are the extruded aluminium side supports and central divider. The inside of the PC boards are etched leaving copper strips 7.5 mm wide (with 2.5 mm gaps) to define the drift electric field. The potentials are provided by current in a resistor chain. Opposite the anode wire there are "diamond shaped" cathode pads [11], which run the whole length of the chamber, and which are used to determine the longitudinal coordinate z (see fig 6).

The cathode pads operate at +4.0 kV, giving an average drift field of 13.4 V/mm, and the anode wire is normally set at +1.85 kV relative to these pads. The field configuration is shown in fig 7. This gives an electric field on the surface of the wire of approximately 1.3×10^5 V/cm. A low drift field is used in order to reduce the maximum voltage anywhere in the system. With this low field the drift velocity depends both on the electric field and on the pressure but as the required resolution is modest this is acceptable and the voltage is easily held sufficiently constant. (Many other drift chamber systems are designed instead to operate in the saturated region.) The drift velocity is approximately 38 mm/μs, and the maximum drift time is 8 μs; after this delay signals are available for the trigger.

Having all the field shaping electrodes, cathode pads and anode wire at a positive potential with a grounded shield on the outside results in positive ions from the avalanches being deposited on the exposed surfaces of the dielectric of the PC board. This has the effect of smoothing the electric field between the shaping electrodes and the overall electric field configuration relaxes to the ideal form required. In these chambers almost 25% of the surface is exposed – they are 25% electrodeless [12] – and charging of the surfaces relies on positive ions coming from the avalanches. Some of this may be provided by the background of natural radioactivity.

The coordinate in the ϕ direction is determined by the drift time to an accuracy of better than 1 mm

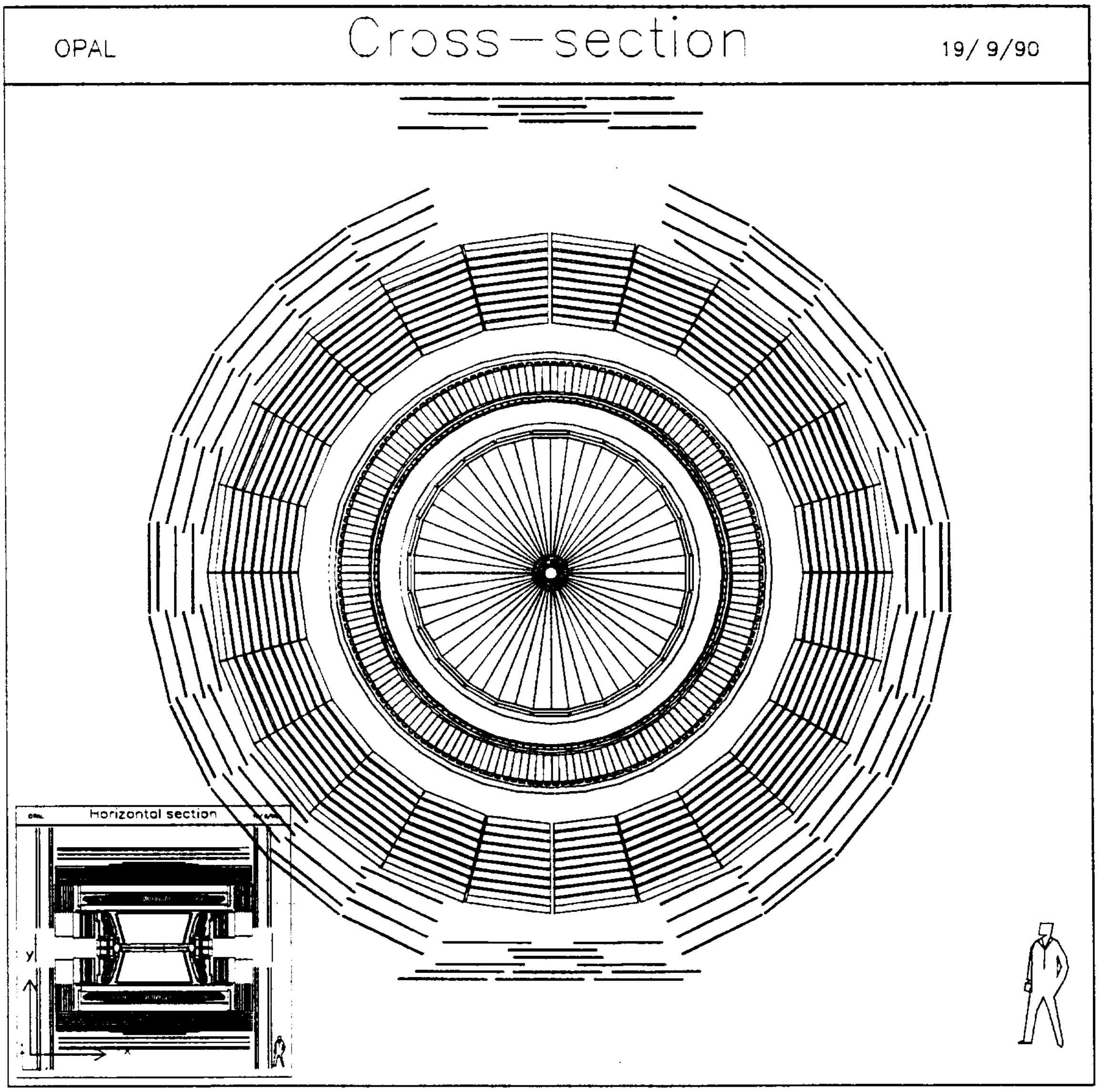

Figure 4: Cross section of the OPAL detector, showing the location of the top, side and bottom muon chambers.

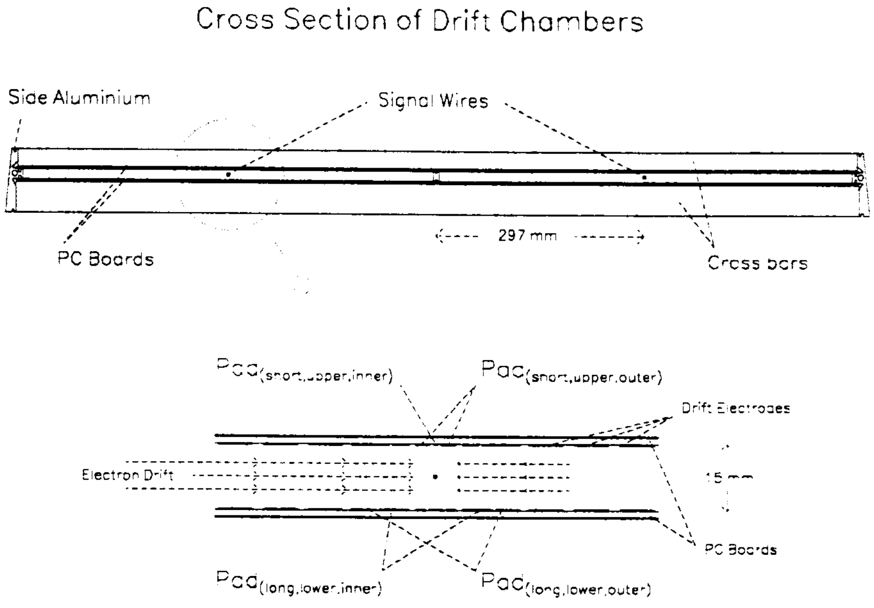

Figure 5: Cross section of a muon barrel drift chamber, showing the two cells.

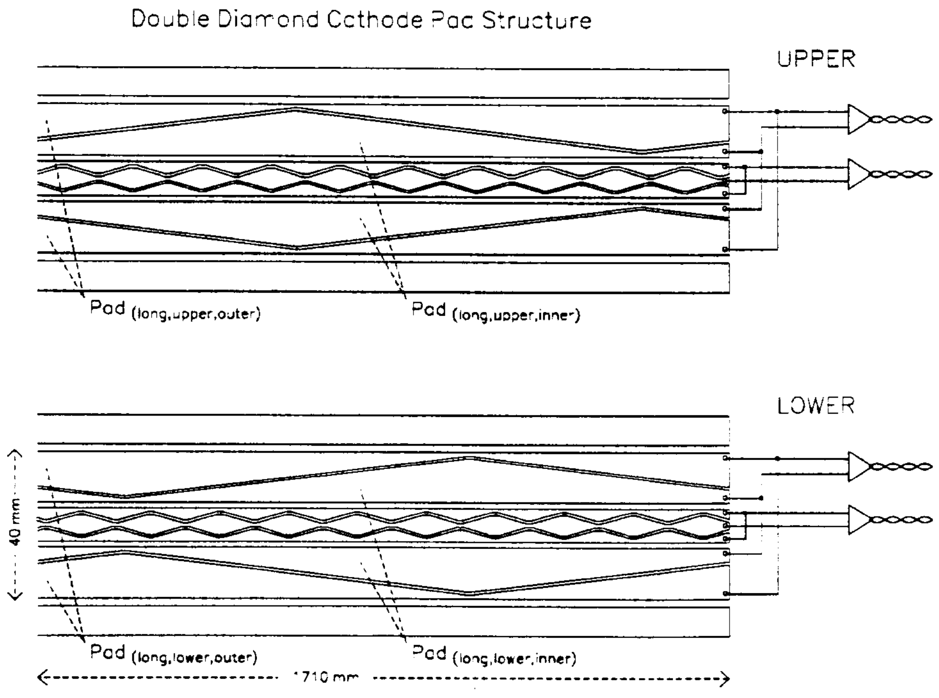

Figure 6: Schematic layout of the diamond shaped cathode pads of a muon barrel drift chamber. Note that, for both the long and the short pads, the phases of the upper and lower repeating patterns differ by a quarter of a wavelength.

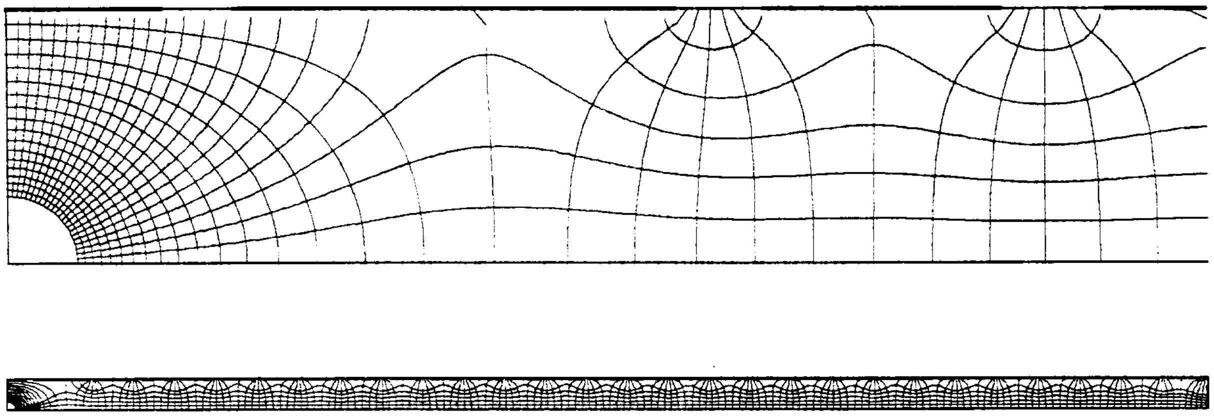

Figure 7: Simulation of the electrostatic field in one quadrant of a drift cell; the wire is at the bottom left hand corner of the plots: Lower: the whole drift distance of 297 mm; Upper: expanded view of region near the wire.

corresponding to a time resolution of about 25 nsec. The chambers also determine the longitudinal coordinate, z. The accuracy is better than 0.02% of 10.4 m for the longest chambers. This is achieved by a three stage process – fine z, medium z and coarse z. The fine z measurement uses diamond-shaped cathode pads with a repeat distance of 171 mm, and determines the z coordinate to an accuracy of 2 mm, but modulo 171 mm. The medium z measurement is based on the same technique but the repeat distance is 1710 mm, and the accuracy about 30 mm. (The dimension 1710 mm is related to the size of PC board commercially available.) The coarse z measurement is obtained by comparing the size of the pulses from the two ends of the wire. The wavelength ambiguities of the fine z measurements are resolved by the medium z measurements and those of the medium by the coarse z measurements [11, 13]. The fine z data are used to calibrate the medium z, and the medium z to calibrate the coarse z.

The wires in the chambers are 10.4 m long for the longest chambers and as the transit time is almost 40 ns the wire is treated as a transmission line. The characteristic impedance is about 300 Ω and this is terminated at both ends to minimise reflections. The wire itself has a resistance of 30 Ω per metre, so the signals as they travel along the wire are strongly dispersed. The shape of the pulse changes as it propagates – the peak amplitude decreases, the width increases only slightly and a long tail developes. Thus a measurement of the height or of the area within a gate of fixed width is sensitive to the distance travelled i.e. to the z coordinate. Strictly speaking this is not charge division (as that requires a deliberate mismatch at the ends and an integration of the charge over several transit times). Moreover the cathode pads can also be considered as transmission lines; the amplitude of the signals depending on the relative width of the pads opposite the avalanche. Again we have attempted to match each of the normal modes of transmission with appropriate resistors at each end. The propagation and matching of such a multi-electrode transmission line is discussed in ref [14].

4.3 Support and survey

The chambers have sufficient mechanical strength to act as their own support and there is no separate independent support structure; each chamber is mounted from the previous layer with simple stand-off brackets. In addition, a 1 mm layer of lead sheet could be added to the outside of the outer chambers, to shield the detector from synchrotron radiation, but this has not been required. The chambers of successive layers are positioned with their readout ends at alternate ends of OPAL (but with the same side facing inwards) in order to calibrate out any systematic effect in the z determination. The structure and installation procedure were designed to be simple and to position the chambers to an accuracy of at best a few millimetres. The actual positions were then determined by surveying, to an accuracy of better than one millimetre. There is a survey button at each of the four corners of each chamber. The position of the wire and the cathode pads relative to these buttons were determined during manufacture. It was found that access to some of the survey buttons was obstructed by the support legs of OPAL and the missing data had to be inferred by other means. Nominally all the sense wires are parallel to the z axis. The coordinates of each button (i.e. the survey data supplied by the CERN survey group) are processed to give for each wire its position, direction and drift direction and these are stored in the OPCAL data base. The tilt of OPAL, 13.9 mrad, has to be included. The internal consistency of the data is at the 2 mm level. It was found that the detector had been installed with a slight twist; i.e. the wires tend to lie on a helix centred about the beam.

4.4 Gas system

The gas used is argon(90%) and ethane(10%), the same as used successfully for the muon chambers at JADE [4], but as the maximum drift distance is now 297 mm instead of 150 mm the purity requirements are more stringent, particularly for the amount of electron attachment during the drift. The drift velocity is required to be constant to better than 0.1%. In order to reduce the consumption of ethane and to allow a large flow, a recirculator is used. The pump, catalyser to remove oxygen and drier to remove water are located on the surface some 100 m above the experiment. One task of the pump is to suck the gas out of the chambers up to the surface against the 4.5 mbar hydrostatic pressure difference. The total circulation is about 1500 litres per hour and the top-up rate of mixed argon/ethane is 250 litres per hour. The pressure at the experiment of the input and output gas is measured with manometers, which also serve as safety bubblers to protect the chambers against over or under pressure. In addition each chamber has its own differential flowmeter (the average flow rate is about 12 litres per hour per chamber).

The oxygen content in the gas leaving the chambers is less than 100 ppm and is much less in the gas entering the chambers. Likewise the water content of the output gas is typically less than 60 ppm (the dew point is less than −50° C) and again much less in the input gas. These critical parameters, as well as several pressures and flows, are are constantly monitored by the slow controls system. In addition there is an unmeasured amount of nitrogen in the circulating gas. The effect of these impurities has been estimated theoretically [15] and the effect on the drift velocity is not significant.

The gas is flammable, but there are only 2.5 kg of hydrocarbon in the whole system. Inevitably the system has leaks; there are over 5 km of gas seal (mostly PC board epoxied [16] to aluminium) in the chambers alone. The measured leak rate is typically 20 to 50 litres per hour over the whole system and this is checked periodically. This leak rate is considered an acceptable hazard provided it is distributed and not localised. Leaks also cause oxygen to enter and contaminate the gas and degrade the electron collection efficiency. The catalyser converts any trace amounts of oxygen in the gas to water. This relies on the 0.5% of hydrogen present in the bottles of ethane. The composition of the top-up gas, which is mixed on site, is constantly monitored using an infra red absorption detector which is calibrated against a reference gas. The fraction of ethane is nominally 10.00% and is kept constant to 0.05%. The chambers are large area and quite flexible implying that the effect of adding gas is to partially blow them up, i.e. a small change in pressure difference between the inside and outside leads to a significant change in volume. This affects the gap in the chamber near the signal wires and thus the electric field and the gas gain, but has little effect on the time of the signal or the sharing between the cathode pads. In practice the pressure differential is maintained at a slight over pressure, 1.1±0.2 mbar, and this gives negligible variation in the gas gain. The top-up gas is added at a constant rate, while the vented gas has both a constant part and a part that is switched according to the pressure difference. The period of the cycle of expansion and contraction is typically about 20 hours. The pressure in the chambers thus follows variations in atmospheric pressure, and this is thought to be the main contribution to variations in the drift velocity. Some effort is required to commission the system at the start of each year of LEP operation, but then little attention is required for routine running and the system runs very reliably for several months at a time.

4.5 High voltage

The computer controlled high voltage system has been specially designed and incorporates hardwired current limits and several fail-safe features. The drift field needs to be stable to about 0.5% in order to achieve the design resolution of 2 mm. There are separate supplies for the drift voltage, V_D=4.0 kV, and the signal voltage, V_S=5.85 kV, for each of the 220 wires and these are computer generated via a DAC with steps of 16 V and 8 V respectively. The actual voltages and currents are read with an ADC every 2 mins and compared with reference values. The status of each wire is stored in OPCAL. The resistor chain for the drift field shaping electrodes draws 17 μA and there has never been a fault in this. At each step there are two resistors in parallel to guard against the possibility that a resistor becomes open circuit. The signal wires draw typically a fraction of a microamp and there is a current limit at 0.4 μA which causes the supply voltage to fall as needed. Of the 220 wires there are only six which draw excessive current or breakdown and these are operated at reduced voltage and thus reduced efficiency. Two of these break down periodically and recover spontaneously.

4.6 Chamber operation

A feature of the construction of the chambers is that there is exposed dielectric inside the chamber. The electric field depends on the charge on these surfaces. At turn on there is initially no charge and the charging up depends on the flux of positive ions coming from the avalanches. Measurements of the singles rates [17] from the cells as a function of time showed that initially the rate (and the current) is anomalously high and it falls to an anomalously low value in about two minutes. Then it takes about five hours for the rate to creep up to its final stable value. This is tentatively interpreted as follows: initially the field at the surface of the wire is high but it relaxes to its final value as charge is deposited in the gaps between the cathode pads thus reducing the gain on a time scale of minutes, thereafter charge is deposited between the field shaping strips and the volume over which the cell is sensitive slowly widens. This is consistent with the total calculated charge being 0.17 nC and a current of about 10 nA flowing for several hours as observed. At OPAL, 100 m underground, the rate of cosmics is about two orders of magnitude less than the rate at ground level but there remains sufficient background and noise for the chambers to charge up as required.

The noise rate is about 10^3 s^{-1} on each cell. In each trigger we expect typically about 2 random hits over the whole of the detector and this causes no confusion with any real track.

4.7 Electronics

The pre-amplifiers on the chambers are purpose built; the schematic circuit is given in ref [18]. At each end of each wire there is a set of resistors which terminate the transmission modes of the signals on the wire and the pads. At one end (D), the current that flows from the wire to the surrounding pads passes through a capacitor and a transformer (to hold off the DC potential), is amplified and sent to the other end (C). At the C end, the four currents that flow between the pairs of cathode pads and the wire current are similarly processed. The signals from the wire, the inner and outer pads have different amplitudes and the gains of the amplifiers are matched accordingly. The signals from the outer pads are the smallest and here noise is a problem. While the wire signals are always positive the pad signals can have either sign (or be zero). The six signals are amplified [18] and sent by twisted pair typically 30 m to the electronics huts. There are only six signals from each cell; 1320 electronic channels in total.

The pulses are digitised in TPDs [19]. These are FASTBUS FADCs developed for the ALEPH experiment, with the input amplifier/shaper redesigned to suit our pulse size and width. They have 8-bit resolution and digitise every 80 ns, the 12.5 MHz clock being supplied from a common external source, which is not synchronised to the LEP RF. A gate, about 8 μs wide, is derived from the beam crossing signal and determines the time window in which signals are recorded. The gate itself is integrated and digitised by one of the TPDs, enabling the time of the chamber signals relative to the beam crossing to be determined to better than 80 ns.

4.8 Data readout

The TPD FADCs digitise continuously and when an OPAL trigger occurs the stored data are frozen and hardware and software in the TPDs searches for hits. If any channel has either its C or its D waveform satisfying the hit criterion then all six waveforms are marked for readout. A hit is defined as at least 2 successive channels being more than 5 counts above the preset pedestal. The part marked for readout includes 10 channels before the start of the pulse (so that the pedestal can be determined later) and 5 channels after the pulse has fallen below threshold. A longer string is marked if necessary. More than one string can be marked for each wire.

4.9 Data acquisition

The data acquisition system consists of FASTBUS front end electronics, read out by two VME based systems (the local system crates), one on each side of the detector. Data are transferred between these systems over a VIC bus. Communication between the FASTBUS and VME systems is via a cable implementation of VSB.

The VME systems use the OS9 operating system and follow the standard OPAL design [20]. Each contains two single card computers, local memory and interfaces to FASTBUS, VIC bus and the OPAL trigger bus. One crate (referred to as the near side crate) contains a second VIC bus interface for transfer of data to the event builder. Data are also sent from this crate to a local VAXstation via an Ethernet connection. The VAXstation is used for local monitoring and online calibration of the detector.

The readout and processing of the data is divided between several tasks which access the data via a buffer manager. Events are buffered in each of the two cpus in addition to a four deep buffer in the TPDs. Readout is handled by two processes running in the first cpu (a CES FIC 8231 with a MC68030 processor). The first stage handles the trigger interrupt and controls event buffering within the TPDs whilst a second stage reads in the event. As these processes run asynchronously, the dead time, 2.5 ms, is governed by the time taken to switch TPD banks, rather than the total readout time which is significantly longer.

The raw data are processed in a second cpu (a Motorolla MVME167 with a MC68040 processor). The raw digitisations are first converted to pulse height information. Two subsequent tasks calculate the coordinate transformation. Data from the near and far sides are then merged and written to a buffer in the VIC bus interface to the event builder. A penultimate stage associates points to form tracks. The final process handles the transfer to the event builder. Events are randomly sampled from this output buffer and sent to the local VAXstation for monitoring and calibration.

The data acquisition chain is controlled by a suite of programs running on the OPAL online VAX cluster. Tasks running on the MVME167 process commands from the run control system and send error messages and status information to the VAX cluster. The high voltage control programs also run on this cpu.

At the event builder, sub-events from the various parts of the OPAL detector are merged and sent on to an HP/Apollo DN10000 (dubbed the filter), where event classification and rejection are performed. This machine also drives the online event display and produces histograms for monitoring. The events are passed on to a network of DN10000 workstations which perform the online reconstruction. A separate workstation is dedicated to producing monitoring histograms of the reconstructed quantities.

For the first year or so of operation, the raw data from the TPDs were recorded with the rest of the data from all the other OPAL sub-detectors so that pulse finding and analysis, as described in section 5, could be rerun offline. However, when the understanding of the detector had improved sufficiently and when the software had became stable and reliable, the analysis was done only online in the VME system and the raw data discarded.

4.10 Trigger

The muon barrel contributes to the trigger [21] of OPAL. 24 trigger signals are generated in parallel corresponding to tracks passing through the chambers in 24 windows in solid angle. Each window extends in θ the whole length of the chambers (no use is made of the longitudinal z information), and spans a minimum of 15° in ϕ. For each sector in ϕ and for each of the four layers the signals from the 2, 3 or 4 cells (that overlap with the 15° sector) are OR'd together. Then for each ϕ sector a coincidence is required from two or more of the four layers. Normally a minimum of three layers are demanded but in some regions where there is poor overlap (as is the case for the edges of the top chambers) or where there are inefficient cells only two layers are required. The purpose built hardware [22] is flexible in that hardware switches enable each cell to be set to on, off or operational, the cells contributing to each OR are programmed in PALs and hardware switches specify whether 2, 3 or 4 layers are required in each sector.

As the drift time extends to 8 μs, this is the effective resolving time and determines the delay to when the trigger becomes available. The singles rate for each cell is typically in the range 0.5 to 1.5 kHz, (and is due mostly to chamber noise). The coincidence rate per ϕ sector is a few tens of Hz where a three fold coincidence is required (but is higher in the few cases where only a two fold coincidence is required). The OR of the 24 signals runs at typically several hundred Hz. The trigger signals are dominated by random events and in practice are used in coincidence with triggers from other sub-detectors. Trigger signals for muons are generated separately for the muon endcap so there is overlap in θ.

4.11 Monitoring

The data from the muon barrel are monitored at various stages through the processing chain. The first level of monitoring is performed by a dedicated VAXstation. This provides the primary means of diagnosing problems in the data acquisition or high voltage systems. Events and high voltage information are transferred from the local system crates. Histograms of pulse-heights and pedestals are produced for each individual readout channel. For each cell of the detector, the drift times, high voltage values, anode wire and resistor chain currents are histogrammed.

Monitoring of the performance of the trigger system is performed by both the OPAL trigger system and by the filter. The latter compares information from the independent trigger and data acquisition systems. Finally the reconstructed hits and tracks can be compared with data from the cental detector using the DST histograms.

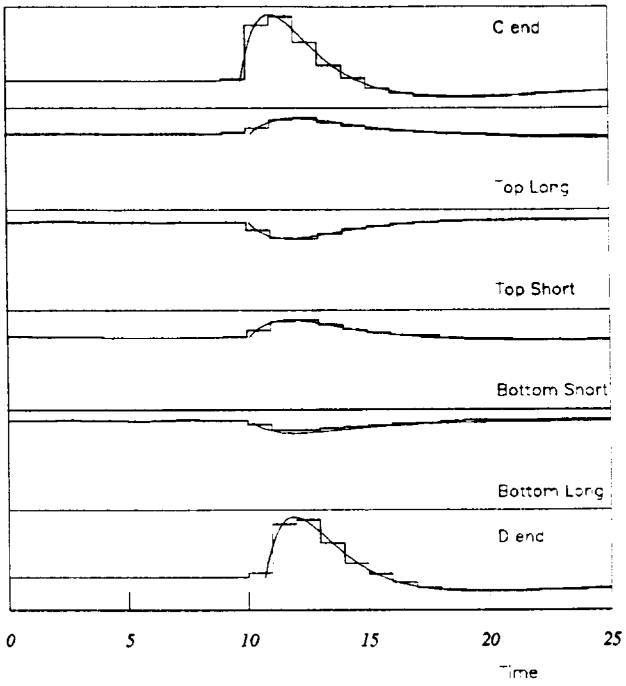

Figure 8: The six waveforms of a typical hit, with fitted curves shown.

5 Analysis of the chamber signals

5.1 Overview

Fig 8 shows the six waveforms digitised by the FADCs for a typical hit i.e. for a single track passing through a single chamber. OPAL events typically contain many such hits and the purpose of the online and offline software is to reject backgrounds and to reconstruct track segments, determining their position and direction in both coordinates. Universal functions are fitted to the waveforms thus determining their time and size. These are used to give the drift distance and the longitudinal coordinate within a cell. The survey data are required to convert to space points in OPAL coordinates and finally these are joined to form track segments. These can be linked to tracks seen in the inner detectors. All this uses algorithms which have been developed and continue to be developed as understanding of the detector grows. Also, many calibration constants are required and these have to be determined, often from the data themselves, and these improve as the understanding improves: it is a somewhat circular process. As well as describing the techniques currently used, this section attempts to indicate, in some instances, how they were arrived at. The description is in terms of the real problems of a real working detector.

5.2 Pulse finding

The first step is to determine how many hits there may be in each FADC string. To investigate this (and the pulse shapes etc) in detail, data (containing about 20,000 pulses) from muon pair candidate events (which contain mostly single clean tracks) were studied. The following algorithm was developed to locate peaks in the FADC sequence and is applied to the C and D wire ends separately. Note that the ADCs are 8-bit linear with a pedestal set nominally at 20.

The first 3 channels in the TPD are averaged to give a pedestal. Further channels are then

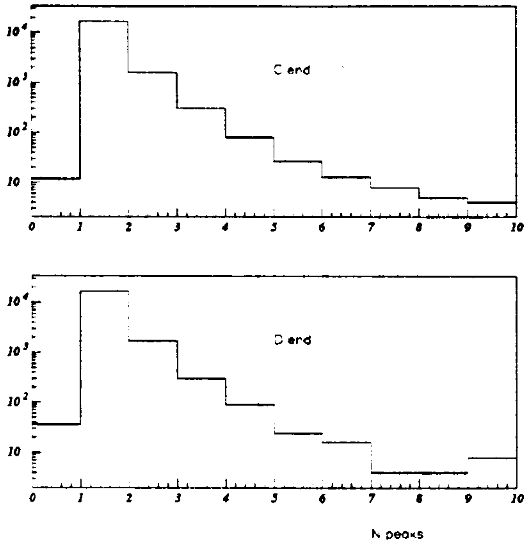

Figure 9: Numbers of pulses found.

considered. If the channel value agrees with the pedestal to within 3 counts, the pedestal is updated and the scan continues. Otherwise a pulse is deemed to have started. Each channel in turn is examined to see whether the pulse is rising or falling. When the slope changes from positive to negative, a peak is deemed to have been found (provided it is at least four channels from the previous one) and a search starts for the next peak.

The numbers of pulses at the C and D ends agreed in 98% of cases and more than half the remainder were ascribable to a small number of chambers with known preamplifier problems. The rest were hits of small amplitude and double hits which were resolved at one wire end but not the other. Most events had single pulses, but there were significant numbers where two or more peaks were found, as shown in fig 9.

5.3 Pulse analysis

For each peak (i.e. hit) found by the method described in the previous section, the time of the wire pulses gives the drift time. The ratio of the pulse sizes (and also the time difference) gives the coarse z coordinate. The ratio of the sizes of the pad pulses gives the medium z and the fine z measurements, and the actual size of the pulse is not important. Extracting the drift time is straightforward and a simple algorithm would suffice. However, to obtain sufficient accuracy in the z measurements, in particular the coarse z which was the most problematical, it was found necessary to fit each pulse to a parametrised form. This also enables multiple hits to be reliably analysed.

Preliminary studies [23, 18] indicated that the wire pulses could be described, to a reasonable approximation, by a *universal* function of two parameters: t_0 describing the time of the pulse, and S giving a measure of the overall size.

$$f_i = Sf(t_i - t_0),$$

Ten different functional forms, including a cubic spline [23], were tried for the wire pulse shape function. All of these basically rose sharply and turned over and fell to cross the axis before turning again to rise slowly towards the baseline as shown in fig 10. The long tail of the pulse is due to the a.c. coupling in the amplifiers. The form which was found to fit the data best was

$$f(t) = t(\beta - t)(1 + \gamma e^{-\delta t})\epsilon^{-\alpha t}.$$

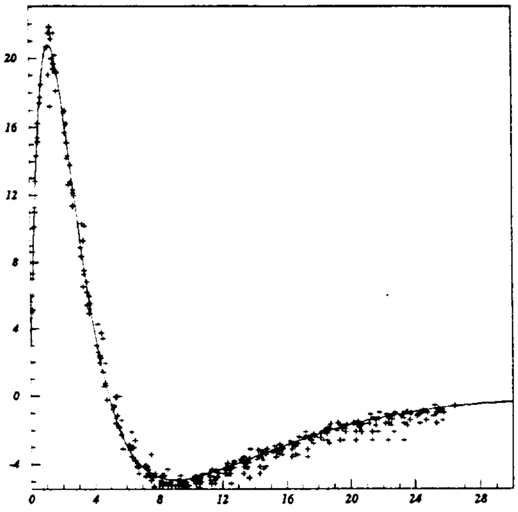

Figure 10: Shape of pulse, fitted function and data points (C end).

The width of the positive part of the pulse is given by β, the decay of the tail by α while γ and δ are shape parameters. The size and time parameters S and t_0 were adjusted for each pulse, pulses that were well fitted were selected and the 4 parameters varied, using the NAG routine E04DGF [24], to give the best overall agreement. The fitted values for the C and D ends were found to be compatible and the best values were

$$\alpha = 0.26 \qquad \beta = 4.9 \qquad \gamma = 8.1 \qquad \delta = 0.34$$

where all times are in clock pulses. These values were then fixed in the code. The curve, together with some data values used in the fit from the C end, are shown in fig 10. Although this form gives a good fit to most pulses, it is not completely trustworthy on the details of the leading edge.

A study was then made of the best way to extract the size and time parameters. The following four levels of complexity were tried:

1. The value of t_0 was taken as the mean value of t for positive values of the pulse, plus a constant 1.45 clock pulses. This last value was adjusted to give the best results. The factor S was fitted in one step using $f_i = Sf(t_i - t_0)$.
2. t_0 was also taken as a variable parameter. The value of S is determined as t_0 is varied. Fitting, using Newton's method, proceeded until the step in t_0 was less than 0.0001 clock pulses.
3. The overall time scale was allowed to vary after the value of t_0 had been found, to allow for the possibility that the width could vary from pulse to pulse: $f_i = Sf\left(X\left(t_i - t_o\right)\right)$. Iteration continued until the change in the factor X was less than 0.0001.
4. t_0 and X were varied jointly, with S determined in closed form as in level 1.

The benefits gained from the more complex levels of fit were compared and weighed against the increased number of iterations required; this is important as the code has to run in the data acquisition system where time is crucial.

The increasing complexity gave an improvement, but more iterations were needed. To reach a decision on which type of fit to use, something more directly useful was required, and this is provided in section 5.5 where coarse z is discussed. It turns out that level 1 fitting is adequate. The code can cope satisfactorily with four or more overlapping hits, providing none are closer than 4 channels, and an example is shown in fig 11.

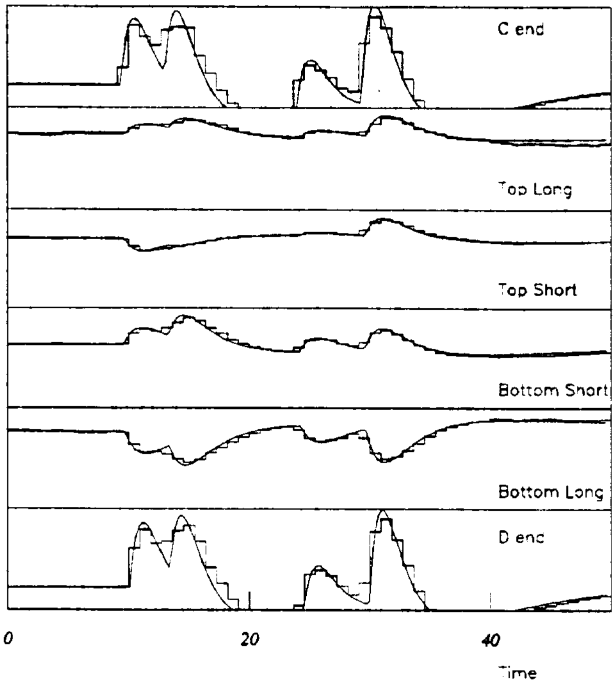

Figure 11: A quadruple pulse - fortunately rare.

5.4 Drift distance

The times of the C and D wire pulses are averaged and the time of the OPAL trigger is subtracted to give the drift time. (The trigger pulse is recorded in one of the FADCs and enables its time to be determined to an accuracy of better than to the nearest clock pulse.) The drift time is converted to the drift distance (the distance of the track from the wire) using a simple linear relation and this requires two constants, the drift velocity, V_{drift}, and a zero-time, T_0. These are determined in the offline calibration. It has not been necessary to invoke a non-linear relation or to allow for special effects close to the wire. A resolution of better than 1 mm is easily obtained corresponding to a drift time of about 25 ns or 0.3 clock pulses. Of course each hit has a left-right ambiguity at this stage.

5.5 Longitudinal measurement, z_c, using wire pulses

The coarse z measurement is obtained from the C and D wire pulses. This section discusses and compares the various ways in which this could be done.

Many quantities, ξ, could be used to obtain a z_c measurement and those studied included:

height: the value of the highest data channel,

area: the sum of the values in the positive part of the pulse,

time: the average time, taken over the positive part of the pulse,

scale(1),(2),(3),(4): the scale factors as determined by the level 1,2,3,4 fits, and

combined: the optimised linear combination of the level 4 scale factor and the time.

The coarse z measurement was determined from these quantities, with a parametrisation of the form

$$z_c = b\frac{\xi_D - a\xi_C}{\xi_D + a\xi_C} + c, \tag{1}$$

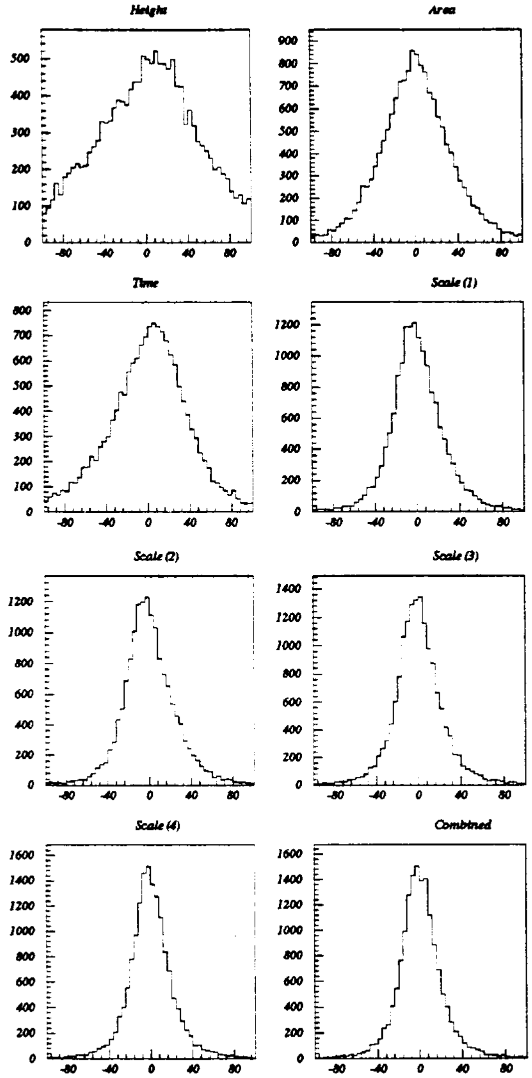

Figure 12: z_c resolution, in cms, for various measures.

(except for the time, where the difference was used without being normalised, and for the combined form). To take account of different amplifier gains the heights etc were scaled so that the averages of the C and D ends were the same, and this determines the constant a. The constants a, b and c were evaluated for each chamber and for each quantity ξ. These values of z_c were compared with that obtained from extrapolating the linked track from the central detector which has an accuracy of a few mms. Results for the z_c resolution are shown in fig 12 for each of the definitions for ξ.

The trends are clear: area is clearly better than height and time, with a resolution (rms) of 34 cm, in agreement with earlier studies [25]. The level 1 scale factor is much better than the area, with a resolution of 26 cm. It can be seen that a level 2 fit is no better than a level 1 fit. A level 3 fit brings the resolution down to 24 cm, and level 4 to 23 cm. Including the time measurement (which one would hope was independent) produces only a small improvement to 22 cm. However, a resolution of 30 cm in z_c is equivalent to a resolution of better than 0.03 clock pulses in the time difference. Moreover, the cable lengths from the C and D ends differ so that for a hit in the middle of the chamber the pulses are digitised with significantly different phase in the FADC. Although timing is often used to extract a longitudinal measurement along a wire, the chambers and electronics were not optimised for this and superior resolution is obtained from the pulse size. It was concluded that the level 1 fit to the wire pulse shapes gives the best overall compromise between accuracy and computing time; as a resolution of 26 cm is adequate. This corresponds to a 'modified charge division' method relying on dispersion as discussed in section 4.2.

An important question concerning the chamber readout has been whether the long negative tails of the pulses contain useful information. To answer this, the z_c resolution was studied using the level 1 fit, but with a cut-off i.e. as a function of the pulse length used (starting from when the signal crossed threshold). It was found that the resolution improves markedly up to a pulse length of about 15, after which there is no further improvement.

5.6 Pad pulses and medium and fine z.

Investigations were also made into the form of the pad pulses. These are simpler to handle than the wire pulses, in that their number and the time, t_0, can be taken from the wire. However, the pad pulses can have positive or negative polarity and can be essentially zero, and are slightly delayed in time due to the different speed of propagation.

A functional form similar to that used for the wire was used successfully, but with the addition of a fifth parameter, ϵ, defining the average difference between t_0 for the C wire end and for the pad pulse. The values adopted for the short pads were:

$$\alpha = 0.155 \qquad \beta = 7.2 \qquad \gamma = 16 \qquad \delta = 0.3 \qquad \epsilon = 0.3$$

and for the long pads:

$$\alpha = 0.13 \qquad \beta = 8.8 \qquad \gamma = 19 \qquad \delta = 0.3 \qquad \epsilon = 0.4.$$

Most pad pulses are simple and give a good fit, like the one shown in fig 8. Fig 11 shows a rather more complicated case where multiple pulses occur. The fitting still does a reasonable job. Further refinement of the fitting algorithms to deal with difficult cases has not been pursued since the fitting procedures developed so far do an acceptable job in almost all cases.

The sizes of the pad pulses are determined by a level 1 fit thus giving for each hit the six quantities Q_C, Q_D, Q_{TL}, Q_{BL}, Q_{TS}, Q_{BS}. (Here TL indicates top-long, BL bottom-long, TS top-short and BS bottom-short.) To estimate z_f and z_m, normalised quantities (which are independent of the overall size of the pulse) are formed:

$$q_{TS} = Q_{TS}/Q \qquad q_{BS} = Q_{BS}/Q$$

$$q_{TL} = Q_{TL}/Q \qquad q_{BL} = Q_{BL}/Q$$

where

$$Q = Q_C + Q_D.$$

The top and bottom pads are periodic and are a quarter of a wavelength out of phase with each other, so the size of the top and bottom pulses have a component which behaves like sine and cosine of the distance along the wire. This applies both to the short and the long pads. A detailed description of the determination of medium and fine z from the pad signals is given in ref [13] which also includes an analysis of the accuracy; here only a brief summary is given.

5.6.1 Fine z – short pads

For the short pads (which determine fine z), the variation with z is harmonic to a good approximation so that the scaled quantities

$$q'_{TS} = a_{TS} q_{TS} - b_{TS} \qquad q'_{BS} = a_{BS} q_{BS} - b_{BS}, \tag{2}$$

depend on z as

$$q'_{TS} \propto \sin \frac{2\pi z}{\lambda_S} \qquad q'_{BS} \propto \cos \frac{2\pi z}{\lambda_S}$$

where. λ_S is 171 mm and the a and b are calibration constants that are determined offline separately for each chamber. Thus the fine z is given by

$$z_f = \frac{\lambda_S}{2\pi} \tan^{-1} \frac{q'_{TS}}{q'_{BS}},$$

where in fact the FORTRAN function ATAN2 is used as this nicely takes care of the signs and gives z_f in the range $-\frac{1}{2}\lambda_S$ to $\frac{1}{2}\lambda_S$. This gives z_f to the required accuracy and no futher refinements are needed.

5.6.2 Medium z – long pads

For the long pads the principle is the same but the procedure is more complicated because the pads are further from the wires and the variation of the size of the pulse with z is no longer approximately harmonic but is almost quadratic within each quarter wavelength:

$$q \simeq C_0 + C_1 z + C_2 z^2. \tag{3}$$

By inverting this, two independent estimates are made for z_m from the normalised charges:

$$z_T = a_{TL} \pm \sqrt{b_{TL} + c_{TL} q_{TL}} \qquad z_B = a_{BL} \pm \sqrt{b_{BL} + c_{BL} q_{BL}} \tag{4}$$

where a, b and c are calibration constants describing the pseudo quadratic behaviour. Here z_T and z_B are measured relative to different origins. Each measurement is used to resolve the sign and origin ambiguities of the other. The ± sign is taken as the sign of c, as the ambiguities are chosen such that in the standard parabolas an increase in z gives an increase in signal.

The accuracies depend on the position along the wavelength (the phase) – the steep part of the parabola gives a better measurement than the flatter part – and the weights are calculated assuming a standard error on q;

$$\epsilon = 4(b + cq)/c^2.$$

The weighted average,

$$z_m = \frac{z_{Tm}\epsilon_T + z_{Bm}\epsilon_B}{\epsilon_B + \epsilon_T},$$

is taken, giving z_m in the range $-\frac{1}{2}\lambda_L$ to $\frac{1}{2}\lambda_L$.

5.7 The combined z measurement

The operation of the chambers in determining the z position of a hit may conveniently be described by noting that the coarse measurement dictates in which of the long pad wavelengths the hit lies, these two together then dictate in which of the short pad wavelenghths it lies, and the short pad measurement then gives the precise value of z. In order to select the correct long wavelength with greater than 99% confidence the resolution of z_c needs to be better than about $\frac{1}{6}\lambda_L$ i.e. 300 mm and likewise the resolution of z_m needs to be better than about $\frac{1}{6}\lambda_S$ i.e. 30 mm. This however is a simplification [26] and a more detailed and sophisticated analysis is given in ref [27].

Suffice it to say that integers, N_m and N_f, are determined such that

$$z_c \simeq z_m + \mathcal{Z}_{mf} + N_m\lambda_L \simeq z_f + N_f\lambda_S$$

within the appropriate accuracies and the latter is taken as the combined value for z.

($\mathcal{Z}_{mf}$ is a calibration constant that takes into account that while the relative position of the short and long pads is well defined on the PC boards there remains an uncertainty in the relative origins of z_m and z_f as determined by the recorded pulses and the software.)

Usually the above procedure is successful and the z of the hit is well determined, but inevitably with a real working detector (of 220 wires and 1320 channels of electronics) there are problems and the chain of hardware and software sometimes fails. Two chambers were found to have a construction error in the layout of the pads, occasionally pre-amplifiers are noisy or misbehave, sometimes tracks are just too close together and some events are cosmic ray showers with hundreds of hits! In some of these cases only limited z information is available and the software indicates this. In practice most hits in useful physics events have a fully reconstructed z coordinate.

5.8 Pulse sizes

While the parameters of interest, drift time and the z coordinates, are, at least to first order, insensitive to the size of the pulses, there is in fact a significant dynamic range in pulse size, and an investigation was made of this. The rms spread in the size of the pulses was found to be about 33% which is much larger than expected from random fluctuations in energy loss (in our gas about 34 primary ionisations [28] are expected in 12 mm, the effective track length) even when allowance is made for other contributions. Studies showed that the pulse size does change with track angle, (i.e. the length of the track in the chamber), but the increase is small and understood. Also it was observed that the signal size does decrease very slightly with increasing drift distance. Fig 13 shows the variation of pulse size for both ends of the wire as a function of the longitudinal coordinate z. There is a large, periodic, variation with z and the repeat distance is not 1.71 m, as would be expected if the problem were connected with long wavelength pads, but is compatible with 1.4 m, which is the spacing of the chamber external supports. The pattern is shared by all three lengths of chamber.

At the positions of large gain, there are wire supports; however these are small, and while they inevitably disturb the electrostatic field, and thus the gain, we expect this to be a small and localised effect. Also located at these positions are the solid aluminium chamber supports which firmly restrict the PC boards of the chamber from bowing outwards due to the slight over-pressure of the gas inside. Between the supports the chambers are known to bow out, thus causing a reduction in electric field at the wire surface and a reduction in gas gain. The scale of the variation in z (i.e. the mean pulse size changes over many centimetres) is consistent with this picture and moreover the calculated change in gas gain is in rough agreement with the observed variation in pulse size.

This variation in pulse size is not in fact a problem, as they appear to behave well in the properties that matter. Resolutions and efficiences are not directly affected as they depend essentially on size ratios. Moreover there is adequate dynamic range in the 8-bit FADC.

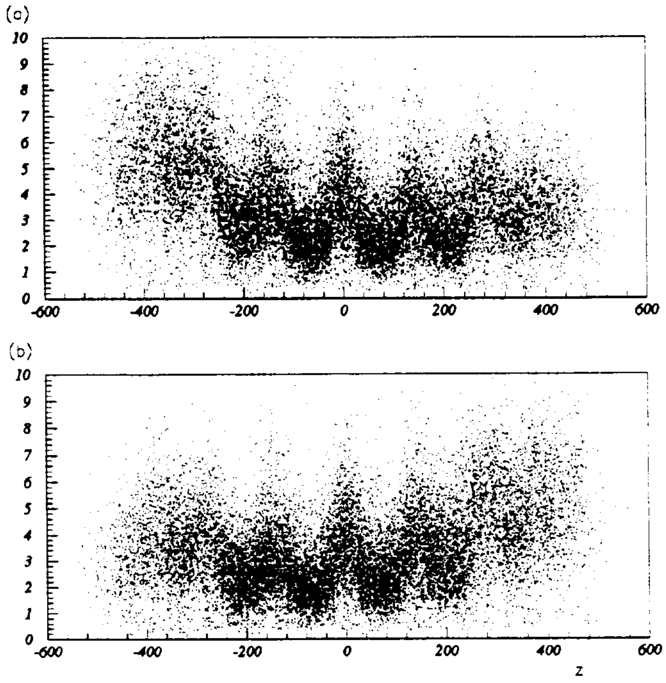

Figure 13: C and D pulse sizes as function of z.

Fig 13 also shows the general trend that pulses are larger for hits near the end from which they are read out. In travelling the 10 m of the chamber the effective change in pulse size is about 50%. It is perhaps impressive that a coarse z measurement relying on changes at the 1 to 2% level can be extracted from pulses that vary in size by almost an order of magnitude.

5.9 OPAL coordinates

The analysis described so far gives x and z, the coordinates of the hit relative to the wire in the particular chamber. These are converted to hit positions (x, y, z) in OPAL coordinates using a set of constants that specify the position and orientation (6 constants) of each of the 220 cells.

5.10 Reconstruction of track segments

The reconstruction of track segments is the last stage of analysis which can be performed online in the VME data acquisition system.

First a fit is performed in the $x - y$ plane, and then the z information is incorporated. The details are as follows.

All hits are considered and any pair of hits which lie within 0.02 rad in ϕ of each other are taken as a starting point for the segment reconstruction. Any subsequent hits found within 20 mm of the two-hit segment direction are considered as belonging to the segment. A straight line fit is then performed to segments with at least 3 hits to give the ϕ position and direction of the segment. The segment is accepted if a) the χ^2 probability of the fit is greater than 0.1%, and b) its direction is compatible with a track originating in the OPAL central region. For regions of the detector where there are less than four layers of muon chambers, two-hit segments are reconstructed if b) is satisfied.

At this stage, some tracks may be found more than once, in that a hit (including left-right ambiguities) may occur in more than one segment. In this case segments with a greater number of hits are accepted over those with fewer, and conditions a) and b) above are used to select the better segment when the number of hits is the same.

Now the z information is included and a straight line fit is performed in the $s-z$ plane (where s is the distance along the segment) to the hits making up a segment in the $x-y$ plane. Initially, only hits with coarse, medium, and fine z measurements are used. This determines the θ position and direction of the segment. If the track satisfies conditions a) and b) above, where this time b) is required to hold in 3 dimensions, then the segment is accepted. Segments with only 2 hits having z measurements are accepted if they satisfy the second condition. If the fit fails however, various steps are taken to try and redeem the situation:

1. The worst point in the segment is dropped, and the fit reperformed. This procedure is continued until the fit is successful or only 3 points remain.
2. There is always a possibility that a hit may have been assigned an incorrect number of medium or fine wavelengths when the z coordinate was determined (see section 5.7). Therefore, when there are only 3 hits left, each is moved by multiples of λ_S and/or λ_L to obtain the best χ^2 segment, where the χ^2 is the combined number for the z track fit and the z measurements.
3. If a 3-hit segment still fails the χ^2 cut, and one point had previously been dropped as the worst point in 1), it is reclaimed and each of the other 3 dropped in turn. The new 3-hit segment is then subjected to procedure 2).

Finally, any hits still left unused because they gave a poor χ^2 or because they were missing some z information (e.g. no medium z coordinate) are considered again. Hits with fine z information are moved by multiples of λ_S and included in the segment if they are close to the segment direction in z. If they had no fine z information, but did have a medium z measurement, they are shifted by multiples of λ_L and included if compatible with the segment direction.

After the fits in $x-y$ and $s-z$ have been performed, other hit ambiguities are considered. A segment may share one hit (the left-right ambiguity is considered as being the same hit) with another segment if the hits fall within the two-hit resolution and were not distinguished, but if 2 or more hits are shared, one segment is probably incorrect. The segment with more hits is accepted, or with the lower χ^2 if the number of hits is identical. If there was one shared hit, and one segment had only 2 hits, or 3 hits and a failed z fit, it is dropped.

The number of hits per segment in a sample of muon pair events is shown in fig 14. It can be seen that most often 4 hits are found, sometimes 2 or 3 due to chamber inefficiencies and occasionally 5 or more when the segment passes through a chamber overlap region.

The endcap region of OPAL is served by a separate sub-detector for identifying muon candidates and this is described elsewhere [3]. Also, the hadron calorimeter [2] supplies additional information on penetrating tracks. Some tracks are identified as segments in more than one sub-detector and where possible these are combined.

6 Calibration

The calibration constants required by the muon barrel detector fall into two classes. Firstly, the constants required for converting the pulse height information to longitudinal coordinates within the reference frame of the individual chambers can be determined from the muon barrel data alone. This first stage calibration is done by a calibration and monitoring program (RAMBO) running on the dedicated online VAXstation, but recalibration offline is also possible. The second class of constants

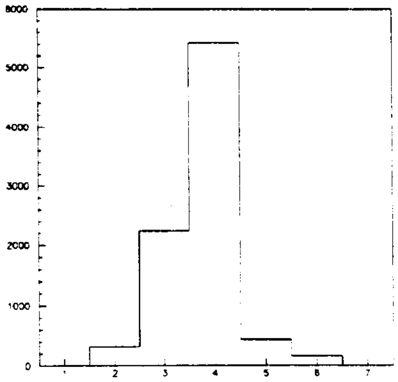

Figure 14: Number of hits found per segment (muon pair data of 1992).

require information from the OPAL detector as a whole and these include the offsets for the longitudinal coordinates and these have to be determined offline where central detector information is available.

The constants for the transverse coordinates (drift velocity and time offset) can be determined by either technique but definitive values are obtained offline.

All the constants are stored in the OPAL data base (OPCAL), as is information on any channels which are faulty, and are used by the offline reconstruction program.

6.1 First stage calibration

The constants needed for the fine, medium, and coarse z coordinate reconstruction are determined by a calibration and monitoring program (RAMBO) running on the dedicated VAXstation.

The chambers are self-calibrating to a large extent, thanks to the presence of intrinsically unalterable distances (171 mm and 1710 mm) in the system, so this can proceed online using data within each chamber. In a sense the fine z information helps to calibrate the medium z and the medium z helps to calibrate the coarse z.

Typically very few changes to the calibration are observed, as in practice these constants only change when a pre-amplifier or FADC module is changed.

6.1.1 Fine z – short pads

This is the easiest and most straightforward of the calibrations. Each chamber needs the 4 calibration constants, $a_{BS}, a_{TS}, b_{BS}, b_{TS}$, (see equation (2) in section 5.6.1) which transform the pad signals q (which have been normalised by the wire signals), into the q'.

These constants relate to differences in the size of the top and bottom pad signals, arising for example from differences in the amplifier gains. The constants also remove an origin shift in both signals, due primarily to the fact that the signal distribution across the split pad is not uniform, but larger nearer the wire.

A plot of q'_{TS} versus q'_{BS} from many events scattered along z should resemble as closely as possible a unit circle centred on the origin. These plots are accumulated and displayed in real time for all 220 chambers and fig 15 shows a typical example. The angle of the line joining the origin to any given point is proportional to the fine z of the hit. While most chambers display good 'circles', a few do not

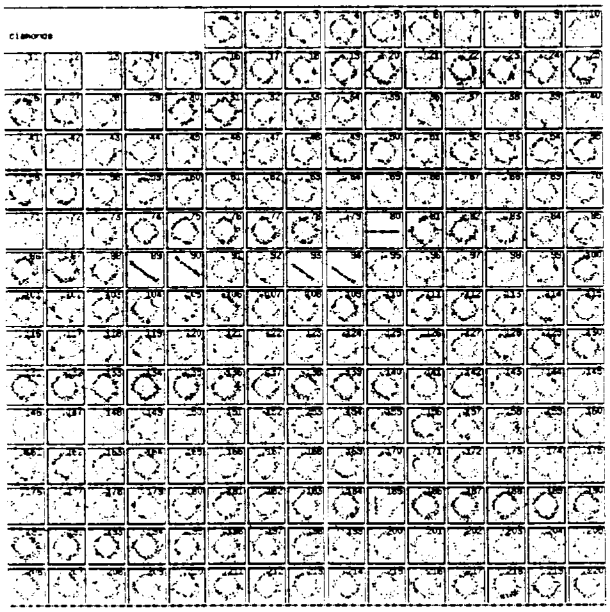

Figure 15: The 220 online calibration 'Circle Plots' for fine z. Each plot has axes q'_{TS} vs q'_{BS}.

and this is due to various hardware faults. For instance the absence of a 'circle' for chamber number 80 in fig 15 indicated a failed pre-amplifier, (which was later replaced).

Starting from the existing calibration, the a and b constants are adjusted until the patterns are symmetric and centred on the origin.

6.1.2 Medium z – long pads

Three constants are needed for the top pads, three for the bottom pads and a seventh constant relates the long pads to the short ones. Fig 16 shows sample scatter plots (just 12 of the 220) of the normalised signals: q_{TL} vs q_{BL}. They differ from chamber to chamber and show nonlinear relationships.

In order to find the constants a, b, c, (see equation (4) of section 5.6.2) of the inverted parabola it

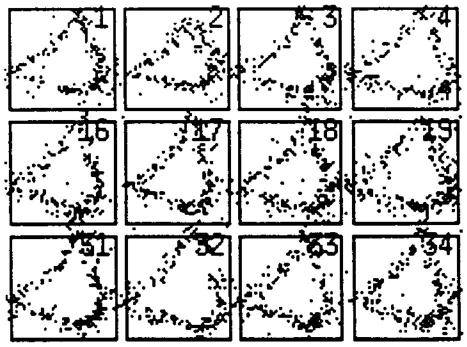

Figure 16: A sample of the 220 online calibration scatter plots for medium z. Each plot has axes q_{TL} vs q_{BL}.

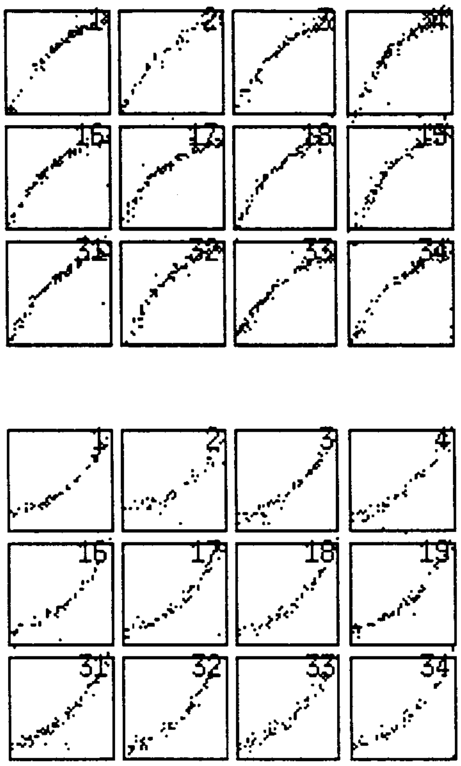

Figure 17: A sample of the 220 online calibration scatter plots for the parabolas of the long pads that determine medium z. In each graph normalised pulse size is plotted against effective z.

is easiest to first determine the parabola constants, C_0, C_1, C_2, (see equation (3)) and these are found by fitting the pad signals, q_{TL} and q_{BL}, as a quadratic function of the longitudinal position. This is obtained from the combined z coordinate – getting precision from z_f, and relying on the starting calibration being good enough to get the right fine wavelength most of the time. Fig 17 shows sample plots of the parabolas for the top and bottom pads. The parameters for the parabolas are then transformed to give the a, b, c constants.

Scatter plots for z_T vs z_B are shown in fig 18. Here, z_T and z_B have been calculated (see equation (4)) from the q_{TL} and q_{BL} using the calibration constants a, b, c. They all have a similar linear (diamond) shape as expected.

The relationship between medium z and fine z is illustrated in fig 19 which also shows the quality of the data. Just 12 of the 220 chambers are shown. Each plot is medium z versus fine z and there

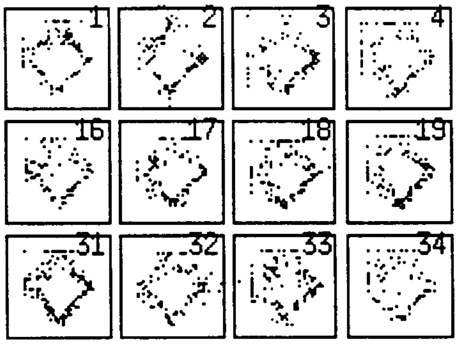

Figure 18: A sample of the 220 online calibration scatter plots for medium z. Each is a plot of z_T vs z_B.

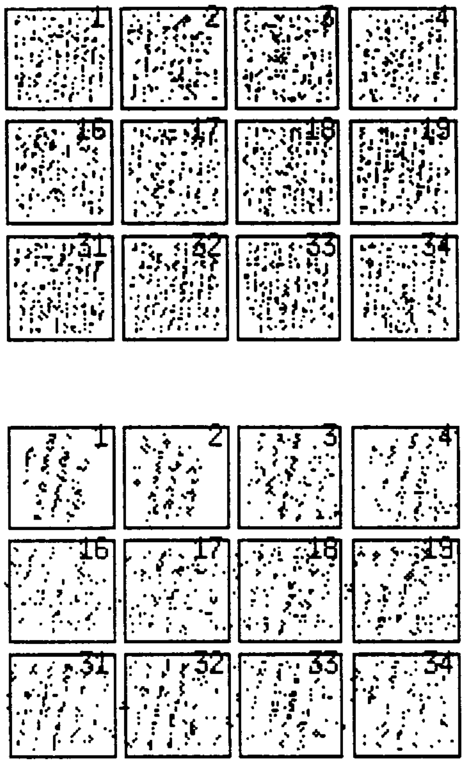

Figure 19: A sample of the 220 online calibration scatter plots: A) Medium z_m vs fine z_f; there should be ten clear bands. B) Coarse z_c vs medium z_m; there should be six clear bands.

should be ten clear bands if the medium z is properly resolving in which short wavelength pad the fine z measurement lies.

Also needed for the medium z is the constant $\mathcal{Z}_{mf}$ which relates the long and short pad coordinate systems. It is determined for each type of chamber (6.0 m, 8.4 m and 10.4 m) from the average difference between the medium and fine z coordinates: $\mathcal{Z}_{mf} = < z_m - z_f - N_f >$.

6.1.3 Coarse z

Each wire has 4 calibration constants describing coarse z. Three of these, a, b, c, are defined by equation (1) in section 5.5. The calibration constant a takes account of any systematic difference in size between the C and D ends that could be caused by differences in electronics. It is evaluated from the averages of Q_D and Q_C. The other two constants b and c are then a slope and constant, and are found by a straight line fit between the quantity $(Q_D - aQ_C)/(Q_D + aQ_C)$ and the complete z. This uses the fact that the complete z has good information in it from z_f and z_m.

A plot of medium z against coarse z should show clear bands if the wavelength ambiguity is being properly resolved and this is shown in fig 19, again for just some of the chambers.

For each chamber, the rms difference between the complete z and the z_c value gives the resolution of the z_c measurement and this is the 4th constant. It is needed for reconstruction when combining the different z measurements and is also a useful diagnostic quantity.

6.2 Second stage calibration

The second stage calibration has to take place offline, some time after the data are taken, as the selection and reconstruction processes must be run on the OPAL event sample. Muon pair events are used for this purpose, as they provide a clean source of tracks (muons of high momentum), passing through the chambers, well reconstructed and little affected by multiple Coulomb scattering in the iron. Tracks from the central detector are extrapolated out to the muon chambers giving the position in each muon chamber to an accuracy of about a millimetre. If a muon segment is found (within a wide tolerance) using the existing calibration, then the differences are found between the extrapolated and reconstructed hits.

In the transverse direction the differences are used to evaluate the drift velocities V_{drift} and T_0 offsets for the chambers. These are not evaluated for individual chambers, but the 4 physical sections (top, bottom, left side and right side) are considered separately, and there are small differences between them. The cause of these differences is not established, but could be due to effects of errors in the survey positions.

An additional calibration constant is needed to relate the longitudinal coordinate as measured by the chamber system to the OPAL coordinate system. This is also done using extrapolations, and a separate value found for each chamber.

This analysis also records the number of times that a hit is and is not found in each chamber on segments linked to extrapolated tracks and this gives an estimate of the chamber efficiency.

6.3 Survey constants

Lastly, constants are required to convert from chamber coordinates to OPAL ones. For this, each of the 110 chambers has four survey buttons, one in each corner, and the positions (x, y, z) in OPAL coordinates of most of these were measured by the CERN survey group. A few were inaccessible and no data were available. These data were found to be internally consistent at the millimetre level and were used to determine the six constants needed for each wire. These are the x and y in the central plane, the position of the chamber along z, the two direction cosines defining the direction of the wire and the angle specifying the drift direction.

7 Performance in OPAL

We define a muon candidate as a track segment formed by hits in the muon detector, which matches the extrapolation of a track from the inner detectors. The matching criteria depend on the type of event being sought. For exclusive muon pairs the criteria are quite lax since the background is small, the danger of misidentification is small and the physics requires a high efficiency. We find that the overall muon pair detection efficiency, including trigger efficiency, within the geometrical acceptance, is $(99.39 \pm 0.12)\%$ [29]. The inefficiency is dominated by track losses of $(0.48 \pm 0.10)\%$ in the central detector. The inefficiency of the muon detectors alone (barrel and endcap combined) is $(0.13 \pm 0.06)\%$. The contamination, mainly $\tau^+\tau^-$ pairs, is $(1.00 \pm 0.11)\%$.

The muon barrel trigger efficiency is shown in figures 20 and 21. The structure is due to gaps for the support legs of OPAL and for cables from inner detectors. The best 54% of 4π has a trigger efficiency of $(99.90 \pm 0.02)\%$, and for 61% of 4π the trigger efficiency is $(98.85 \pm 0.13)\%$. Note that the muon barrel trigger demands hits in 3 or more layers over most of the geometrical acceptance (see section 4.10), and this implies that individual chambers have an efficiency of 98.7% for detecting high energy muons.

Finding muons in multihadron events is more demanding. Often muons (and electrons) are used to enrich a data sample with heavy quark events. The standard OPAL analysis criteria are defined in references [30] and [31] and in outline are:

1. The matching inner detector track is required to have momentum greater than 3 GeV/c to ensure it has enough energy to penetrate the iron of the return yoke.

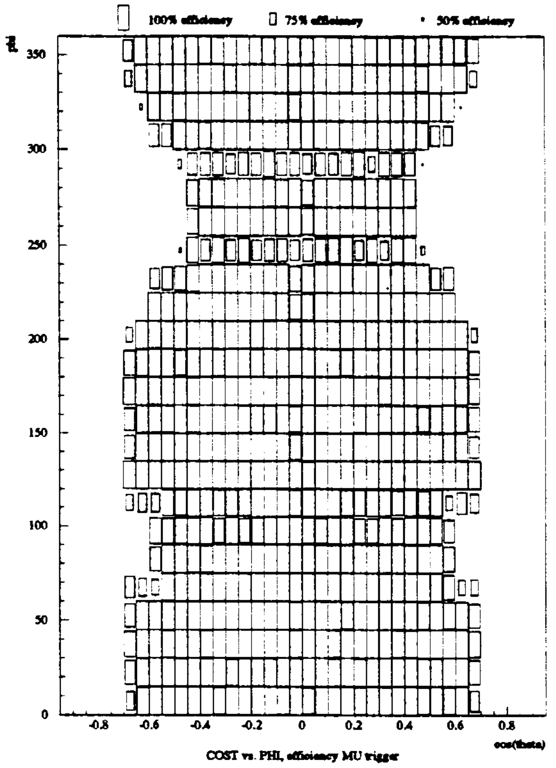

Figure 20: Muon barrel trigger efficiency; $\cos\theta$ vs ϕ. (The top chambers are at a ϕ of 90 degrees.)

2. The deviation in azimuthal and polar directions of the muon track segment from the extrapolated track, taking into account errors on the extrapolation from both measuring and multiple scattering and measuring of the muon segment, is limited by a χ^2 cut which accepts most muons as determined by exclusive muon events.

3. A track is excluded if there is a shower of more than 20 nearby muon track segments — this is taken to indicate hadron punchthrough and avoids misassociation.

4. In the case of multiple association the track is excluded unless the secondaries are statistically very unlikely — this further mitigates against punchthrough.

Under these circumstances the overall muon detection efficiency for barrel and endcap combined, including geometrical acceptance, is found to be $(76 \pm 3)\%$, where the error is systematic. The probability that a hadron seen in the inner detector, with momentum greater than 3 GeV/c (and momentum component transverse to the thrust axis greater than 1 GeV/c) fakes a muon is $(0.47 \pm 0.01)\%$, where here the error is statistical [30]. This varies from about 0.6% at low momentum to 0.3% at high momentum, is almost independent of transverse momentum and is well modeled in our simulation program, which has been tested with $K^0 \rightarrow \pi^+\pi^-$ and $\tau \rightarrow 3\pi$ decays. Also, we find, in the above circumstances, that approximately 11% of the muon candidates in hadronic events are fakes [31]. Of these, roughly 66% are from decays of hadrons in flight, 15% are from hadron punchthrough and 19% from hadron sneakthrough and misassociation.

8 Summary

After five years of running the OPAL muon barrel subdetector at the LEP collider it is apparent the main goals have been achieved. The efficiency for finding track segments is high, well over 99% for

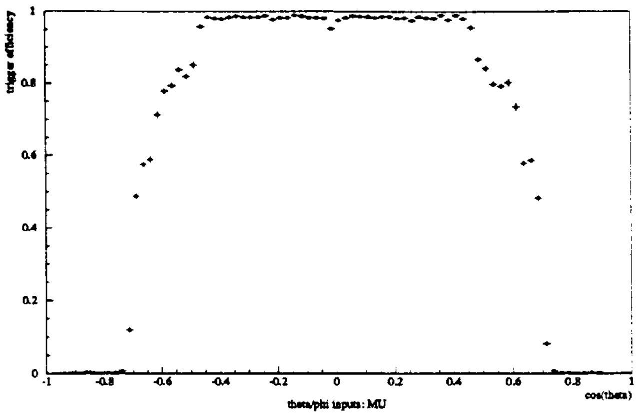

Figure 21: Muon barrel trigger efficiency vs $\cos\theta$.

clean tracks where there is coverage and the spatial and angular resolutions are as required by the original specification. The technology chosen is still a good match to the physics environment and requirements and five years on we would probably still choose the same solution. The low rates at LEP allowed a long maximum drift time and surprisingly few electronic channels (only 1320 for 220 wires). Optimisation in the design and development stage led to a rather simple mechanical design but some sophistication in the electronic read out. As with many other detectors the survey turned out to be more of a problem than anticipated. The pattern recognition and determination of calibration constants required a significant software effort. It might also be mentioned that the original design was for the drift coordinate only but as the project developed it was found possible to include the longitudinal coordinate essentially at no extra cost for the hardware.

At turn on some six cells of the 220 were found to not stand full volts and these are operated at reduced efficiency. However there has been no further signs of deterioration which is encouraging as this detector is required to operate for another five or more years!

The main limitations of the detector have turned out to be the unavoidable problems of holes in the solid angle coverage due to poor overlap between the top and side chambers (dictated by access), support legs for the OPAL magnet and other holes for cable runs for other sub-detectors.

Acknowledgements

We wish to thank the many engineers and technicians, from Manchester, RAL and CERN, without whose dedication and skill this project would not have been possible. We are indebted to DESY, and in particular to H.Kessler, for providing the gas recirculator. We gratefully acknowledge financial and technical support from The Science and Engineering Research Council (now The Particle Physics and Astronomy Research Council), UK and The University of Manchester. We have enjoyed the hospitality of CERN and the warm working atmosphere of the OPAL collaboration.

References

[1] The OPAL detector technical proposal, CERN/LEPC/83-4.

[2] K.Ahmet et al., The OPAL collaboration, Nucl. Instr. and Meth. A305 (1991) 275-319. The OPAL detector at LEP.

[3] G.Arnison et al., Nucl. Instr. and Meth. A294 (1990) 431-438. Production and testing of limited streamer tubes for the end-cap muon subdetector of OPAL.

[4] J.Allison et al., Nucl. Instr. and Meth. A238 (1985) 220-229. The JADE muon detector.

[5] J.Allison et al., Nucl. Instr. and Meth. A238 (1985) 230-237. Muon identification in JADE.

[6] In the coordinate system of OPAL the x axis is horizontal and points approximately towards the centre of LEP, the z axis is in the e^- beam direction (which makes a small angle to the horizontal) and the y axis is approximately vertical. The polar angle, θ, is measured from the z axis and the azimuthal angle, φ, from the x axis about the z axis. In this paper the z coordinate of a chamber refers to measurements along the wire (which nominally are parallel to the z axis of OPAL.)

[7] I.Duerdoth, Manchester University Prepreprint, MAN/HEP/91/03 (1991). A pointing theorem for tracks in a cylindrically symmetric magnetic field.

[8] J.Allison et al., Nucl. Instr. and Meth. A317 (1992) 47-74, The detector simulation program for the OPAL experiment at LEP.

[9] A.K.Amundsen et al., Nucl. Instr. and Meth. A293 (1990) 145. The control system of the OPAL detector at LEP.

[10] Norplex UK Division, UOP Ltd. Feltham, Middlesex, UK.

[11] J.Allison et al., Nucl. Instr. and Meth. A236 (1985) 284-288. Diamond shaped cathode pads for the longitudinal coordinate from a drift chamber.

[12] J.Allison et al., Nucl. Instr. and Meth. 201 (1982) 341-350. An electrodeless drift chamber.

[13] J.Allison et al., Nucl. Instr. and Meth. 310 (1991) 527-534, and London Conference on Position-sensitive detectors, 1990 Sept 4-7. The diamond shaped cathode pads of the OPAL muon barrel drift chambers.

[14] I.Duerdoth, Manchester University Preprint, MAN/HEP/91/02 (1991). Multi-electrode transmission line.

[15] S.Biagi, Nucl. Instr. and Meth. A283 (1989) 716-722, A multiterm Boltzmann analysis of drift velocity, diffusion, gain and magnetic-field in argon-methane-water-vapour mixtures, and private communication (code of MAGBOLTZ program).

[16] Flexovoss K6T from Bondaglass-Voss Ltd, Beckenham, Kent, UK.

[17] I.Duerdoth, Manchester University Preprint, MAN/HEP/90/03, (1990). Charging and discharging of the OPAL muon barrel drift chambers.

[18] G.Bahan, Manchester University Preprint, MAN/HEP/91/05 (1991). Pulse simulation and the longitudinal coordinate in the OPAL muon barrel chambers.

[19] B.Lofstedt, CERN Preprint, CERN-EP-EL, 89.04.13, TPD Time Projection Digitiser F6821.

[20] J.T.M.Baines et al., Nucl. Instr. and Meth. A325 (1993) 271. The Data Acquisition System of the OPAL Detector at LEP.

[21] M.Arignon et al., Nucl. Instr. and Meth. A313 (1992) 103-125. The trigger system of the OPAL experiment at LEP.

[22] We acknowledge support from the CERN (in particular C.Virtue) and Saclay groups in the design and implementation of the trigger hardware electronics.

[23] S.Pawley, Investigation into the resolving power of the OPAL muon drift chambers for double hits. Diploma Report, Manchester University (1989).

[24] The NAGLIB Library mark 15, The Numerical Algorithms Group. Oxford (1991).

[25] A.J.P.O'Dowd, Charge-time analysis in the OPAL muon chambers. Diploma Report. Manchester University (1988).

[26] P.Hinde, Investigation of the parameters affecting the resolving power of the OPAL muon drift chambers. Diploma Report, Manchester University (1987).

[27] R.Barlow, Nucl. Instr. and Meth. A349 (1994) 277-280. The longitudinal coordinate from 'Double Diamond' tapered cathode pad readout.

[28] P.Rice-Evans, in 'Spark, Streamer, Proportional and Drift Chambers', Richelieu, London (1974), quotes a figure of 27.8 primary ionisations/cm for argon.

[29] R.Akers et al., OPAL Collaboration, Z.Phys. C61 (1994) 19-34. Improved measurements of the neutral current from hadron and lepton production at LEP.

[30] P.D.Acton et al., OPAL collaboration, Zeit Phys C69 (1993) 19-35. The forward-backward asymmetry of $e^+ + e^- \to b + \bar{b}$ and $e^+ + e^- \to c + \bar{c}$ using leptons in hadronic Z^0 decays.

[31] P.D.Acton et al., OPAL collaboration. Zeit Phys C58 (1993) 523-539. Measurement of $\Gamma(Z^0 \to b\bar{b})/\Gamma(Z^0 \to hadrons)$ using leptons.